IOP Publishing Physica Scripta
Phys. Scr. 95 (2020) 035509 (10pp) https://doi.org/10.1088/1402-4896/ab51ed

Magnetic field detection using a highly sensitive FBG probe

Alireza Samavati[1,4], Zahra Samavati[1], Ahmad Fauzi Ismail[1,4], Noorhana Yahya[2], Mohamad Aizat Abu Bakar[1], Mohd Hafiz Dzarfan Othman[1], Mukhlis A Rahman[1], Khong Nee Koo[1] and Siti Sarah Osman[3]

[1] Advanced Membrane Technology Research Centre (AMTEC), Universiti Technologi Malaysia, 81310 UTM, Johor Bahru, Malaysia
[2] Department of Fundamental and Applied Sciences, Universiti Teknologi Petronas (UTP), 32610, Bandar Seri Iskandar, Malaysia
[3] Laser Center, Ibnu Sina Institute for Scientific and Industrial Research, Universiti Teknologi Malaysia, 81310 UTM Johor Bahru, Johor, Malaysia

E-mail: alireza.samavati@yahoo.com and afauzi@utm.my

Received 1 August 2019, revised 20 October 2019
Accepted for publication 28 October 2019
Published 6 February 2020

Abstract

A partially unclad fiber Bragg grating (FBG) coated with Fe_3O_4 nanoparticles as a magnetic field sensor is experimentally demonstrated. A series of six FBGs reflecting different wavelengths at an efficient length of 30 mm are fixed on the top and outside of a cylindrical glass chamber. The chamber is equipped with a solenoid that acts as a magnetic field generator and is filled up with air, saline solution, and crude oil separately to detect the changes in the magnetic field. The magnetic–hysteresis loops confirm the super-paramagnetic properties of the synthesized Fe_3O_4 nanoparticles with size smaller than 20 nm. The sensor response time of ~21 s confirms the high reliability and repeatability of the sensing scheme. The change in the magnetic field strength depended from FBG–solenoid distance, propagating at different media and function generator frequency leads to shift in the reflected wavelength of each single FBG's accordingly. The magnetic field strength outside the solenoid obeys the inverse-cubic law, and the decrease in the wavelength shift with an increase in the FBG–solenoid distance is in excellent agreement with the Biot–Savart law. The shift is caused by the interference of different propagating modes that are reflected from the core-cladding and cladding-magnetite layer interfaces; these modes have different phases because of the changes in the refractive index of the magnetite layer resulting from the change in the magnetic field. Our precise fabrication of the FBG probe with a maximum sensitivity of ~11 000 pm mT^{-1} and the proposed design of experiment may be appropriate for detecting small changes in magnetic fields in the oil industry.

Keywords: fiber Bragg grating, magnetic field sensor, optical fiber, solenoid

(Some figures may appear in colour only in the online journal)

1. Introduction

Precise monitoring of magnetic field altered by the environment has attracted extensive attention for usage in a variety of applications such as biomedical detection and controlled nuclear fusion as well as in the oil industry, military, and so on [1–4]. In recent years, owing to the unique advantages of magneto-optical sensors such as small size, high resolution, and definitive precision, these sensors have been widely used [2, 5]. An optical fiber containing a Bragg grating can reflect a particular wavelength of light and can be used in many applications. The excellent features of the fiber Bragg grating

[4] Authors to whom any correspondence should be addressed.

(FBG), in particular its sharp spectral response make it suitable for application in devices in which the accurate control of wavelength is desired.

The FBG can be used in multiplexing optical telecommunication as a wavelength-selecting device in dense wavelength division and in fiber laser resonator and many types of optical sensors such as flowmeter for measuring the fluid flow [6]. Magnetic fields play an important role in fields such as geophysics, defense, medicine, and the oil industry. The existing techniques to detect magnetic fields involve solutions such as search coils, fiber optics, flux-gate magnetometers, and Hall-effect sensors [7].

When employing fiber optics, a change in the magnetic field change is sensed by detecting the intensity, phase, polarization, and wavelength modulation of the propagated light. The Faraday effect [8], Lorentzian force [9], Fabry–Perot [10], Mach–Zehnder [11] and magnetostrictive effect [12–14] in an interferometry arrangement are employed to demonstrate magnetic field detection by the fiber optics. The photodetector detects the propagated light, which is modulated once the probe is exposed to a magnetic field, by encoding the perturbed polarization state of the light and converting it to intensity- and wavelength-based data. Usually, the encapsulation of an FBG with a magnetic fluid and the attaching magnetostrictive material to FBGs are the two common techniques for fabricating magnetic field sensors. The changes in the refractive index of nanofluid and the mechanical expansion of magnetostrictive materials due to exposure to a magnetic field cause a shift in the reflected wavelength, enabling the probe to act as a magnetic field sensor [15, 16]. According to a recently published review, FBGs were encapsulated by different ferrofluids such as Fe_3O_4, EMG 507, EMG 607, and EMG 605 for magnetic field detection. It was reported that both magnetic field directions, namely, the perpendicular and parallel to the fiber axis can be sensed and that the maximum sensitivity was $\sim$10 000 pm mT^{-1} when EMG 607 was used [17]. However, in this research, the systematic partial removal of the cladding and the accurate deposition of small magnetite nanoparticles was found to improve the sensitivity of the probes. Normally, magnetic sensors are fixed inside a solenoid or permanent magnet to observe the effect of a changing magnetic field [18–20]. However, in our research, the probes detect the magnetic field from outside the solenoid. The advantage of this technique is that the magnetic field strength outside the solenoid is much weaker than that inside, and therefore, our probe should be sufficiently sensitive to detect the weak magnetic field. The oil tertiary recovery process through effective interaction of nanofluid with oil and rock in porous media at the presence of magnetic field can increase the yield and profit in the oil and gas industry. High sensitive magnetic field sensor is prerequisite for *in situ* monitoring of the oil movement in porous media which leads altering the magnetic field strength [21]. Therefore, our suggested optical fiber probe is highly capable for application in oil and gas industry specifically in enhanced oil recovery process.

In this study, a series of six partially uncladded FBGs coated with Fe_3O_4 nanoparticles were fixed on the top and outside of a cylindrical glass chamber to detect different magnetic field strength. This glass chamber was equipped with a solenoid at the chamber end and in the center. The wavelength shifts in the reflectance spectra were chosen as the target for sensing, and they were detected by using an optical spectral analyzer. Appropriate characterization techniques were employed to describe the probe morphology, magnetic properties of the coated material, and performance of the sensors.

2. Sensor design and principle

2.1. Fabrication of FBG magnetic probe

The FBG was fabricated from single-mode glass fiber optic having 8.2 and 125 μm core and cladding diameter respectively. The operational wavelength domains of the FBGs were chosen so that these domains did not overlap (λ_B for FBG1 = 1534 nm, FBG2 = 1544 nm, FBG3 = 1547 nm, FBG4 = 1550 nm, FBG5 = 1552 nm, and FBG6 = 1554 nm). The cladding material is silica doped by fluorine with refractive index of 1.4500 $\pm$ 0.0025, and core is made of silica with refractive index of 1.4765 $\pm$ 0.0025. The excimer laser (Lambda Physik, Germany; Model Compex 110) in the order of $\pm$1 beam was operated at 193 nm wavelength, 50 Hz, 100 mJ pulses and pulse duration of 10 ns. The fibers were exposed to the intense UV light for duration of 300 s to complete the Bragg grating inscription. The period of the phase mask grating corrugation was 1072.6 nm. By varying the distance between phase mask and target fiber optic, we managed to inscribe Bragg grating having length between 10 and 30 mm.

The fabricated optical sensor system is realized partially removing the FBG cladding following by coating the removed part by magnetite nanoparticles. The thickness of remaining fiber cladding part should be less than 2 μm according to the penetration depth in the infrared (IR) region. The process of removing the cladding should not interrupt the total internal reflection and light propagation through the core. Therefore, to determine the appropriate optimum etching time, the transmission intensity was dynamically monitored during the immersion of the fiber in a 30% HF solution at temperature of 15 °C. The weak HF acid was used to prevent core surface corrosion that can cause a huge loss in light propagation. By monitoring the light intensity spectrum, the optimum immersing time was found to be 57 min at room temperature, and only $\sim$650 nm thickness of the cladding remained. The rate of etching is found to be $\sim$1.06 μm min^{-1}. This diameter was chosen because the evanescent light field can penetrate through the FBG cladding into the surrounding medium and causes changes in the light properties in response to an external magnetic field.

Then, every single partially unclad FBG was subjected to magnetite coating by using a polymer agent as the adhesive element. For this purpose, Fe_3O_4 nanoparticles were fabricated by co-precipitating ferric chloride ($FeCl_2$, sigma Aldrich) and ferrous chloride ($FeCl_3$, Qrec) in the presence of

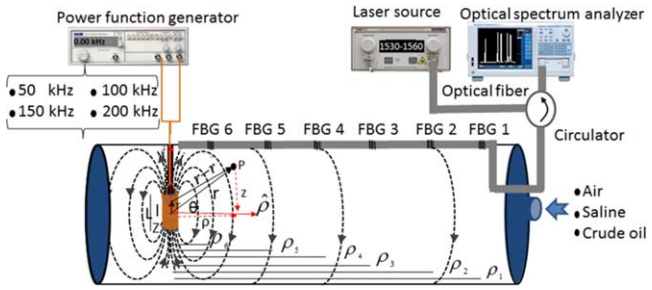

Figure 1. Schematic diagram of the experimental setup showing the parameters for calculating the magnetic field outside the solenoid.

N_2 gas. First, 6.34 g of ferric chloride and 16.23 g of ferrous chloride powder were dissolved in 200 ml distilled water. Chemical precipitation occurred at 30 °C under continuous stirring of the solution for 30 min and addition of 2 M sodium hydroxide. The reaction system was then kept at 70 °C for 3 h, and the pH of the solution was ±12 at equilibrium. The black precipitate obtained was cooled to room temperature by removing the heat source and was separated by a using permanent magnet. The precipitate was rinsed with distilled water and ethanol several times until the pH of the product became neutral. Then, the obtained precipitate was dried in a vacuum oven at 60 °C for 24 h to obtain the final form ready for coating. For the preparation of the polymer coating agent, 20 g poly(methyl methacrylate) (PMMA) pellets (Chi Mei Corporation) were first dissolved in a tetrahydrofuran (THF, Merck) solution with 20 wt% of PMMA. The PMMA pellets were completely dissolved in THF after stirring for 24 h at 50 °C. Then, 10 g of the synthesized Fe_3O_4 nanoparticles were then added into the PMMA solution; then, the solution was stirred for 1 h and sonicated for another 1 h to achieve a uniform dispersion state. After the mixture was ready for coating, the etched FBG was dipped into the mixture and dried in air for a few minutes. The dip-coating process was repeated thrice, and the coated fiber was dried in the vacuum oven for 24 h at 40 °C. The low-temperature treatment is necessary to completely remove the THF solvent at a slow evaporation rate as well as to enhance the adhesivity between the nanoparticle-embedded cladding and fiber. After all the FBGs are coated, they were spliced to a bare fiber optic with similar structure by using a fiber optic cleaving device (FC-6S High Precision Single Fiber Cleaver) and a fiber optic fusion splicer (Sumitomo Z1C) in series configuration. Then the complete fiber sensor was placed in 6 mm diameter polyurethane tube and fixed on the surface of the chamber by epoxy glue. The experimental setup is shown schematically in figure 1. A simple air cooling system was provided to prevent any potential heating issue at the solenoid. The solenoid was placed inside a thermal insulation polymer tube to avoid residue heat transfer from solenoid to the system.

2.2. Characterization methods

A field emission scanning electron microscope (FESEM, JEOLJSM 6380LA) equipped with an energy dispersive x-ray spectrometer (EDX) were used to observe the deposited magnetite layers and analyze the element existing in the probe structure. A broad band source with a laser wavelength ranging from 1300 to 1700 nm and an optical spectrum analyzer (OSA) (ANDO AQ6317B) were used as the light source and detector, respectively. A room-temperature vibrating sample magnetometer (VSM, Lake Shore 7303-9309 VSM) was employed for determining the magnetic properties of the magnetite nanoparticles. For time response test, a sensing signal was originated by a tunable laser with a wavelength of 1544.140 nm, corresponding to the Bragg wavelength of the FBG2. The reflection power variation was detected by a partial discharge and recorded via a data acquisition card via Lab VIEW program with a sampling frequency of 100 Hz.

2.3. The principle of magnetic field component

In our design of experiment, the solenoid is set vertically at the end–middle of the chamber to generate a magnetic field. The solenoid produces a magnetic field perpendicular to the chamber axis. The magnetic field strength is tuned by using a power function generator. The schematic diagram in figure 1 shows the parameters used to calculate the axial component of the magnetic field B_z in the Cartesian coordinate system. At distances much larger than L (the length of the solenoid), the entire solenoid itself is treated as a point magnetic dipole [22]. The axial component of the field at point P is calculated as follows:

The solenoid has n turns per unit length. For a loop of infinitesimal thickness $\frac{-t}{(t^2+\rho^2)^{3/2}}$ along the axis, a current $nI\mathrm{d}z'$ flows through this loop. The magnetic moment of this loop is determined as $\vec{m} = nI\mathrm{d}z'\hat{z}$. The magnetic field of this point dipole is as follows:

$$d\vec{B}(\vec{r}-\vec{r}') = \frac{\mu_0}{4\pi}\frac{3(\vec{m}.(\vec{r}-\vec{r}'))(\vec{r}-\vec{r}')-\vec{m}}{(\vec{r}-\vec{r}')^3}. \quad (1)$$

Here, the permeability of free space is μ_0, and r is the vector from the coil element to point P, as shown in figure 1. It is assumed that the solenoid is located along the z-axis and extends from $-L/2$ to $L/2$.

The radial component of the field at point P due to the coil element at z' is given below:

$$\mathrm{d}\vec{B}_\rho(\vec{r}) = \frac{3nIA\rho\mu_0}{4\pi}\frac{(z-z')}{(\vec{r}-\vec{r}')^3}\hat{\rho}. \quad (2)$$

Because of symmetry, the radial component of the field vanishes for an infinite solenoid; meanwhile, for a finite solenoid, this component is small and ignorable. The axial field at point P due to the coil element at z' is given as follows:

$$\mathrm{d}\vec{B}z(\vec{r}) = \frac{nIA\mu 0\mathrm{d}z'}{4\pi}\left(\frac{2(z-z')^2-\rho^2}{(\vec{r}-\vec{r}')^5}\right)\hat{z}. \quad (3)$$

To find the net field at P, we integrate the previous expression for magnetic field between the limits $z' = L/2$ and $z' = -L/2$.

$$\vec{B}_z(\vec{r}) = -\frac{nIA\mu_0}{4\pi}\int_{z+t/2}^{z-t/2}\left(\frac{2t^2-\rho^2}{(t^2+\rho^2)^{3/2}}\right)\mathrm{d}t. \quad (4)$$

This integral can be exactly solved by substituting $t = \rho \tan\theta$. The anti-derivative of the integrand in equation (4) is $\frac{-t}{(t^2+\rho^2)^{3/2}}$. Thus, we get the following expression:

$$\vec{B}_z(\vec{r}) = -\frac{nIA\mu_0}{4\pi}\left[\frac{z - L/2}{((z - L/2)^2 + \rho^2)^{3/2}} - \frac{z + L/2}{((z + L/2)^2 + \rho^2)^{3/2}}\right]. \quad (5)$$

On one hand, by considering the positions of the FBG, it is concluded that Z is constant for all six FBGs and only the distance from the center of the solenoid coil differs among them. These distances are shown as ρ_1–ρ_6 in the schematic diagram. The magnetic field strength is seen to be a function of the inverse cube root of ρ. Therefore, the magnetic strength that reaches the FBGs decline as an inverse cube.

On the other hand, magnetic field is affected as it propagates through different media, and its direction lines change. Magnetic susceptibility indicates the magnetic flux. The higher the magnetic susceptibility, the better is the magnetic flux with lower attenuation. For instance, the density of magnetic force lines is reduced in the presence of diamagnetic materials and vice versa for paramagnetic materials. Such change in the magnetic field inside a substance is described as follows. In the SI system, equation (6) represents the change in magnetic field inside a medium:

$$B = \mu_0(H + M), \quad (6)$$

where H and M are the magnetic field strength and intensity of magnetization of the media, respectively. In order to investigate the effect of the medium through which the magnetic field propagates, it is appropriate to employ a parameter independent of the magnetic field. Thus, after dividing equation (6) by H, we obtain the following:

$$\mu = \frac{B}{H} = \mu_0 + \mu_0\frac{M}{H} \quad (7)$$

$$\frac{M}{H} = \chi_V, \quad (8)$$

where μ is the relative permeability, and χ_V is the dimensionless coefficient of the volume magnetic susceptibility. The specific or mass magnetic susceptibility (χ_m) is another informative parameter:

$$\chi_m = \frac{M_m}{H} = \frac{\chi_V}{\rho}[10^{-8}\ \mathrm{m^3\,kg^{-1}}]. \quad (9)$$

It is the ratio of mass magnetization (M_m) to the magnetic field (H) or the ratio of the volume magnetic susceptibility (χ_V) to the density (ρ) of the medium. For the magnetic field outside a solenoid,

$$B \propto \frac{1}{\chi_m}. \quad (10)$$

Therefore, the approximate amount of magnetic field in air (empty chamber), saline solution, and crude oil was calculated. The results are shown in figure 2. The mass magnetic susceptibility for the saline solution and crude oil was −0.89 and −0.99 (10^{-8} $\mathrm{m^3\ kg^{-1}}$), respectively [23]. It is clear that changing the chamber liquid from air to saline solution and from the saline solution to crude oil, the magnetic field strength diminishes.

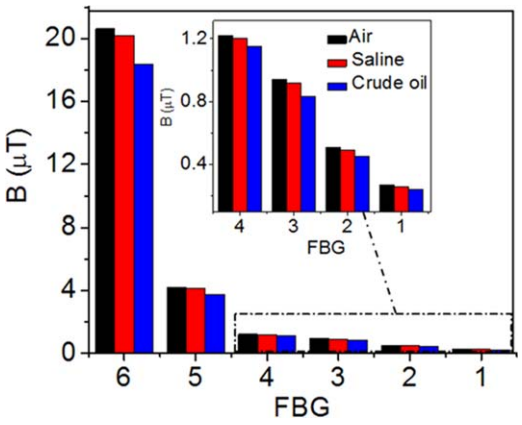

Figure 2. Magnetic field strength received by FBGs (calculated using equation (5)) after filling the chamber with different liquids.

In this experiment, the magnetic field strengths were generated by using a loop of radius 3 cm and a constant current of 1 A. The field strength is higher at higher frequencies. This observation agrees with the theory that at higher frequencies, the loop radiates an electromagnetic field more effectively. However, at higher frequencies, the attenuation is remarkably greater, resulting in considerable lowering of the maximum operating range. The very low frequencies of 200 kHz magnetic waves can penetrate inside the medium up to depth of 1 m. For deriving the frequency-dependent formula for magnetic field strength, we start with the Maxwell's equations for propagating wave-like solutions at a specific point. Given the vector and scalar potentials, the associated electric and magnetic fields can be evaluated using the following well-known equations:

$$E = -\frac{\partial A}{\partial t} - \nabla\varphi \quad (11)$$

$$B = \nabla \times A. \quad (12)$$

If the radius is much greater than λ, the average power of the wave that cross a spherical surface S for a single period of oscillation can be determine as follows:

$$P = \oint_s \langle u\rangle.\mathrm{d}s, \quad (13)$$

where the Poynting flux is given by

$$u = \frac{E \times B}{\mu_0} \quad (14)$$

$$u = \frac{\varepsilon_0 E^2}{2} + \frac{B^2}{2\mu_0}. \quad (15)$$

Here, E and B wave are defined as follows using θ and ϕ as the standard spherical polar coordinates aligned along the z-

axis:

$$E \simeq -\frac{wlI_0}{4\pi\varepsilon_0 c^2}\sin\theta\frac{\sin[w(t-r/c)]}{r}\hat{\theta} \tag{16}$$

$$B \simeq -\frac{wlI_0}{4\pi\varepsilon_0 c^2}\sin\theta\frac{\sin[w(t-r/c)]}{r}\hat{\varphi}. \tag{17}$$

After replacing E and B waves in equation (14), the total energy flux of the EM wave across the spherical surface at a specific point P is found to depend on the square of the frequency of the generator:

$$P_P = \frac{\omega^2 l^2 I^2}{12\pi\varepsilon_0 c^3}, \tag{18}$$

where C is the velocity of light; l is the length of the antenna; and ω is the frequency. As expected from the energy conservation principle [24] the total flux is independent of radius S. Therefore, increasing the frequency itself enhances the energy reaching the FBGs.

The refractive index of the magnetite nanoparticles can be tuned by the external magnetic field. In the first-order approximation, the dielectric constant is linearly proportional to the magnetization. In the dielectric tensor $\varepsilon(M, \omega)$, only ε_{xy} pair of diagonal elements is non-zero when M is in the z direction. The ε_{xy} components in the first-order approximation of magnetization vary linearly with M and increase the magneto-optical effects. The refractive indices depend on magnetization and can be expressed as follows [25–28]:

$$n^2 = aM + b \tag{19}$$

$$M = \chi_{V\,(\text{magnetite})}H, \tag{20}$$

where $\chi_{V(\text{magnetite})}$ is the volume magnetic susceptibility for magnetite; a and b represent the proportionality constants, and M is the magnetization. It can be concluded that exposing the magnetite to an external magnetic field causes magnetization of the ferromagnetic materials. By changing the magnetization using different external magnetic fields, the refractive index of the magnetite nanoparticle can be varied.

2.4. The interference principle based on coated partially unclad FBG

When the light encounters two reflective parallel surfaces, at every internal reflection, one portion is reflected and the remaining is transmitted. Multiple beam interference occurred as these beams are bounded. This phenomenon can be explained by the Fabry–Perot interferometer principle. In our experimental setup, the two interfaces are the core-cladding and cladding-magnetite thin film. After recombination, the difference in the optical path lengths of these two spectra that were reflected from two different interfaces resulted in constructive and destructive interferences depending on the phase variance. The interference spectrum was determined by using the following two-beam interference equation:

$$I = I_1 + I_2 + 2\sqrt{I_1 I_2}\cos\left(\frac{2\pi L\Delta n_{\text{eff}}}{\lambda} + \varphi_0\right). \tag{21}$$

Here, I is the intensity of the total interference signal detected by the spectral analyzer. I_1 and I_2 are the intensities of the light reflected by the core mode and cladding modes, respectively, as shown in the schematic diagram in figure 3. Here φ_0 is the initial phase difference; L, the length of the sensing part; and λ, the wavelength. Further, Δn_{eff} is the difference between the effective RI of the core mode and cladding modes:

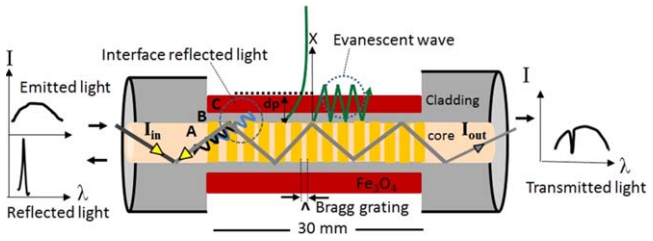

Figure 3. Schematic diagram of the FBG probe structure and sensing mechanism based on interferometric study of core and cladding mode spectra.

$$\Delta n_{\text{eff}} = n_{\text{eff}}^{\text{core}} - n_{\text{eff}}^{\text{clad}}. \tag{22}$$

Equation (21) shows that the maximum transmission occurs when

$$\frac{2\pi L\Delta n_{\text{eff}}}{\lambda} + \varphi_0 = 2m\pi + \varphi_0, \tag{23}$$

where m is an integer. Therefore, the transmission spectrum reveals dips at the following wavelengths:

$$\lambda_m = \frac{L\Delta n_{\text{eff}}}{m}. \tag{24}$$

The changes in the external magnetic field does not affect $n_{\text{eff}}^{\text{core}}$, and it is almost unchanged; however, following equation (25), $n_{\text{eff}}^{\text{clad}}$ with changes in the external magnetic field strength. Therefore, any small change in the external magnetic field caused by differences in variables such as distance, media, and power frequency leads to changes in $n_{\text{eff}}^{\text{clad}}$ and Δn_{eff}. Therefore, the dip wavelength shift $\Delta\lambda_m$ can be written as follows:

$$\Delta\lambda_m = \frac{(\Delta n_{\text{eff}} + \Delta n)L}{m} - \frac{\Delta n_{\text{eff}}L}{m} = \frac{\Delta nL}{m}, \tag{25}$$

where Δn is the difference between the effective RI of two states corresponding to different magnetic field strengths. Considering equation (25), it can be concluded that the varying of sensing length L and differences in RI, i.e. Δn can both result in a detected light wavelength shift. When L is constant (15 mm), the wavelength shift is a linear function of the changes in RI. Therefore, all the above mentioned phenomena and mechanisms indicates that any change in the strength of the magnetic field propagating along a chamber can modify the RI of the thin magnetite layer and consequently lead to a wavelength shift.

3. Results and discussion

Figures 4(a) and (b) shows the FBG reflection peak and the full width at half maximum of a single FBG as a function of

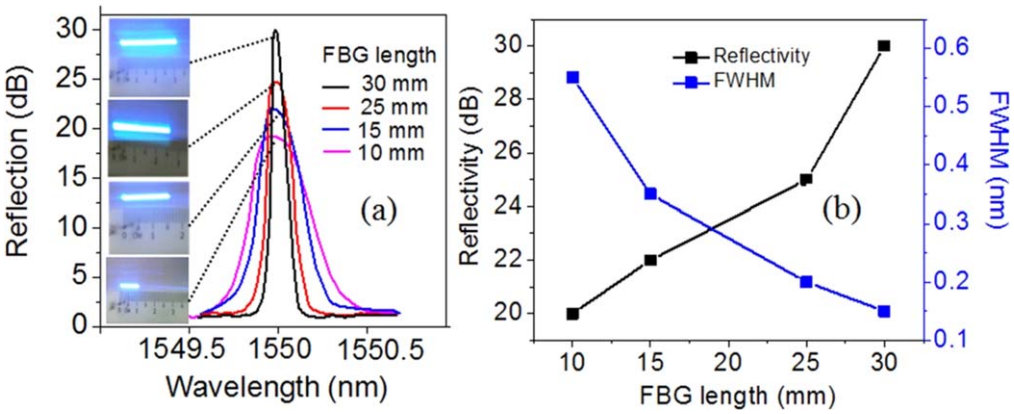

Figure 4. Reflected spectra of FBGs of different lengths (a). Reflectivity and full width at half maximum of the reflection spectra as a function of the length of the FBG (b).

length. Figure 4(b) shows that the reflection intensity is enhanced upon increasing the length from 10 to 30 mm. It can be seen that the FWHM of the reflection signal is inversely proportional to FBG length. The manner of insertion of the FBG into the structures determines the spatial resolution of the parameters detected by FBG as a sensor. These parameters can be the refractive index, strain, vibration, temperature, and magnetic field. The FBG sensors have better stability against strain gradients as the grating length decreases. Moreover, to increase the spatial resolution of the measurands, the FBG must be as short as possible. However, longer FBGs provide better reflection and lower reflection attenuation. Therefore, an experiment was conducted to investigate the dependence of FBG characteristics such as FWHM and reflection maximum on the FBG length. By employing different phase mask lengths exposed to an excimer laser, single-mode FBGs of different lengths were fabricated. Theoretically, the reflection maximum can be calculated using the following formulas [29]:

$$\lambda_B = 2n_{\text{eff}}\Lambda \tag{26}$$

$$R \propto \tanh^2(\alpha L), \tag{27}$$

where λ_B, n_{eff}, and Λ are the Bragg wavelength, effective refractive index of the fundamental mode, and the grating pitch, respectively. L is the FBG length, and R is the maximum reflection intensity. Equation (27) implies that upon increasing the length of an FBG, the reflection maximum is enhanced, however, as mentioned earlier, further increasing the length leads to lower strain stability. The experimental results agree with the above mentioned theory of the FBG. Therefore, in this study, 30 mm long FBGs were used to fabricate the sensing probes.

The top-view and cross-sectional FESEM views of the FBG sample coated with magnetite nanoparticles are shown in figures 5(a) and (b), respectively. The inset in figure 5(a) shows the EDX mapping of the FBG surface. The high-magnification TEM image of the selected area is shown in figure 5(c). Homogeneous dispersion of magnetite nanoparticles with an average size of ~10 nm is clearly confirmed from figures 5(a) and (c). The cross-sectional view reveals that the cladding was successfully removed, and only ~650 nm thickness of cladding remained, thereby enabling better interaction of the propagating light with the external media. The thickness of the magnetite nanoparticle coating on the partially removed cladding was ~250 nm. When total internal reflection occurred at the core/cladding interface, the light was not reflected back completely at the interface, and some light penetrated into the cladding material. This portion of the light is called the evanescent wave, and its intensity exponentially decays as a function of the distance from the interface [30]. The penetration depth (d_p) of the evanescent wave in the cladding material is given by equation (28), and it is associated with the incidence angle θ, refractive index of the core, n_1, and that of the cladding, n_2, and the wavelength of light.

$$d_p = \frac{\lambda}{2\pi(n_1^2 \sin^2\theta - n_2^2)^{1/2}}. \tag{28}$$

Considering the above formula, when the wavelength of the light is 1550 nm, the penetration depth of the evanescent wave is ~2 μm, thus confirming that removing a major part of the cladding until only ~650 nm of thickness is left (figure 5(b)) allows the evanescent wave to reach the coated magnetite particles.

The output of VSM measurement for magnetite nanoparticles at room temperature (300 K) indicates a hysteresis curve of magnetization with the magnetic field which is depicted in figure 6. Notably, a small remanent magnetization of less than 3%, which indicates a super-paramagnetic behavior, is observed. Therefore, our magnetic field sensor based on a probe coated with magnetite nanoparticles has excellent repeatability. From the hysteresis curve, the value of saturation magnetization (Ms), remanent magnetization (Mr), and coercivity field (Hc) of the magnetite nanoparticles were determined, as shown in the inset of figure 6.

The effect of magnetite thin film thickness and magnetic field direction are investigated using VSM analysis. Figures 7(a) and (b) show magnetic–hysteresis (*M–H*) loops for magnetite film having variety of thicknesses measured with magnetic field aligned in perpendicular and longitudinal direction towards the films plane respectively. It can be seen from figure 7(a) that the film expose to perpendicular

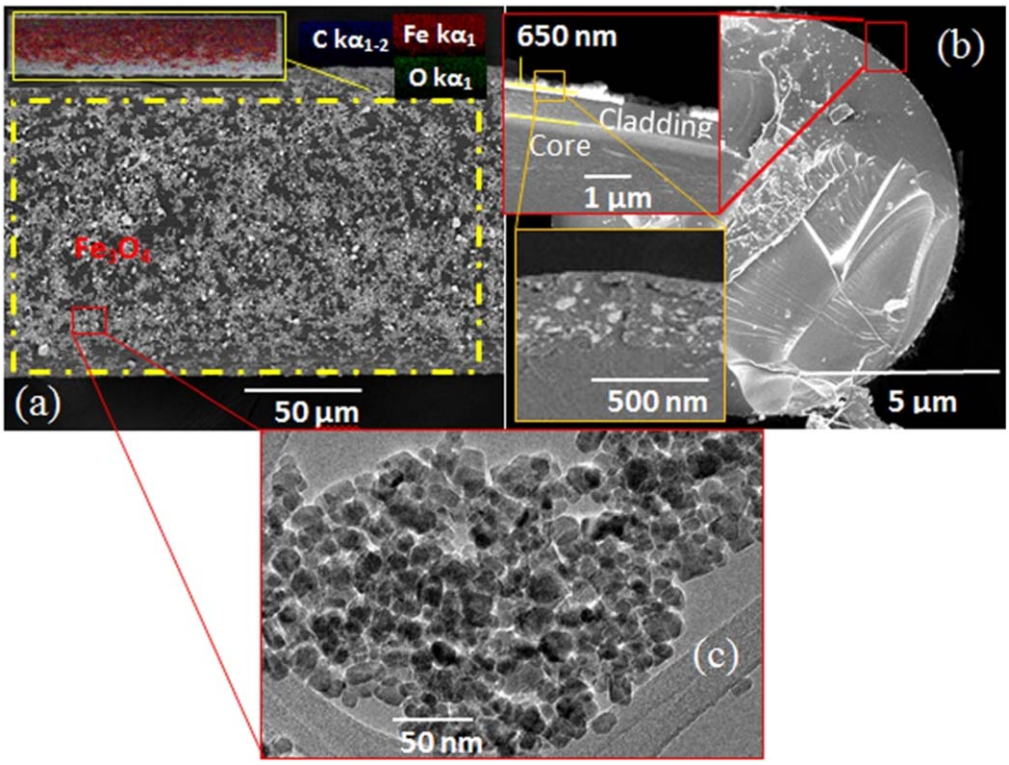

Figure 5. Top-view FESEM image of the coated partially unclad FBG with magnetite nanoparticles (a). Inset shows the EDX mapping of the selected area. The cross-sectional view of the partially unclad FBG (b). Inset shows a highly magnified view of the selected area. The TEM image of the selected area (c) showing the deposition of magnetite nanoparticles on the FBG.

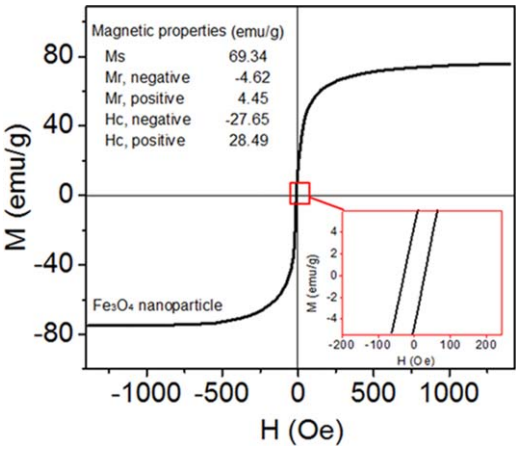

Figure 6. Magnetic–hysteresis (*M–H*) loops of Fe_3O_4 nanoparticles. Inset: High magnification view of a selected area showing the small hysteresis loop, indicating a ferromagnetic component.

magnetic field is not depend on the film thickness. However, for magnetic field longitudinal to the film the loop depends on the thickness. The remanence to saturation magnetization (Mr/Ms) versus thickness curve (inset on the right) experiences an increase with the film thickness growth up to 15% (for the 150 nm thick film) followed by a subsequent drop for thicker films and keep constant for more than 250 nm thickness. In our experiment according to the magnetic field direction outside the solenoid which is perpendicular to the film plane the magnetization does not have significant changes by varying the thickness.

Figure 8(a) shows the reflection spectrum from a series of six FBGs when the chamber is empty (air) and function generator is off (zero magnetic field). The order of the FBGs is shown in the schematic diagram. The wavelength shift for every FBG at a different frequency is shown in figures 8(b)–(d) when the chamber is filled with air, saline solution, and crude oil, respectively. The three phenomena can be understood from these plots. First, the wavelength shifts for almost all FBGs increase as the distance from the solenoid decreases. Second, the light reflected from the FBGs shows a smaller shift when the chamber is filled with saline solution or crude oil than when it is filled with air. Finally, when the frequency is increased from 0 to 200 kHz, the wavelength shift increases. These phenomena are attributed to the fact that the magnetic strength magnitude reaching the magnetite nanoparticles varies with distance, media, and frequency which are theoretically explained in section 2.3. These differences cause changes in the refractive index of the coated magnetite. The mechanism of the changes in the refractive index and wavelength shift upon varying the magnetic field is described comprehensively in the following text.

Figure 9 shows the wavelength shift of FBGs for chambers filled with different media. The sensitivity varied with the medium. As can be seen from figure 9(c), the FBG probe yielded better performance for a function generator frequency of 200 kHz when the chamber was filled with oil. The sensitivity of the probe depends on not only the manufacturing process (for instance, the accuracy of the removing process for cladding and the homogeneous coating of small

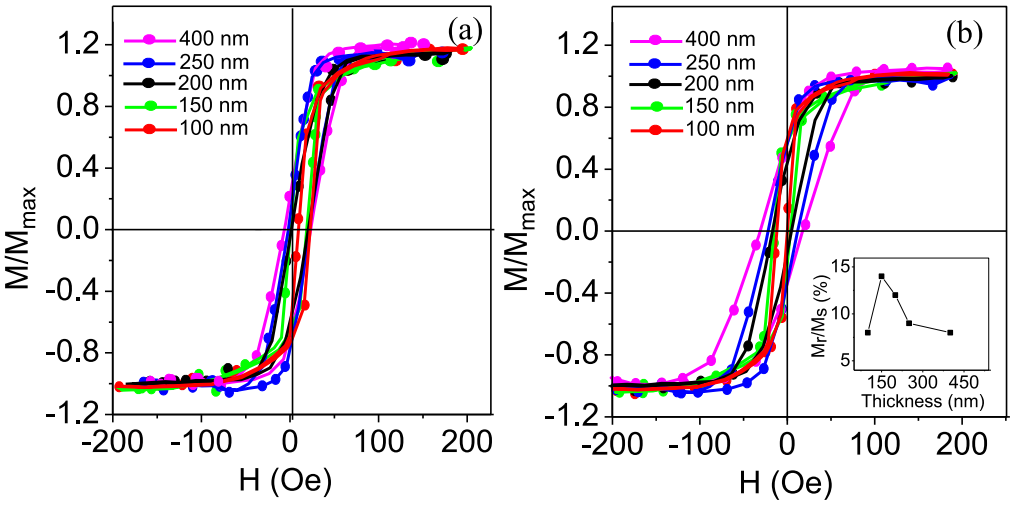

Figure 7. Magnetic–hysteresis loops for 100, 150, 200, 250 and 400 nm thick magnetite thin films measured via VSM at room temperature with perpendicular (a) and longitudinal (b) direction applied magnetic field towards the films plane. The inset show Mr/Ms of the films thickness when magnetic field is longitudinal to the films.

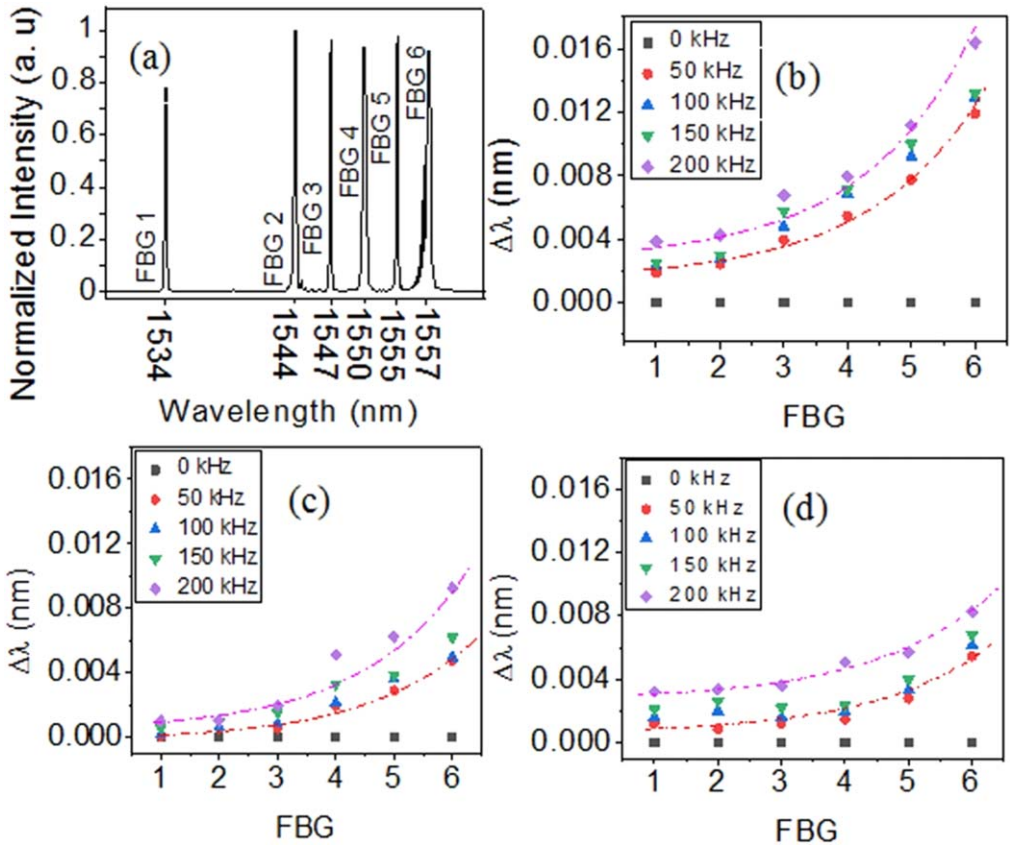

Figure 8. Reflected spectra of six FBGs in series configuration (a), wavelength shift of the FBGs after filling the chamber with air (b), saline solution (c), and crude oil (d).

magnetite nanoparticle on the partially unclad part), but also the magnetic field intensity received by the FBG probe. For higher frequencies of function generator, the sensitivity is higher, and vice versa. From the *M–H* hysteresis loop shown in figure 6, the saturation magnetization of magnetite nanoparticle is ~69 emu g^{-1}, and its absolute coercive force is ~28 Oe. This value is still beyond the magnetization saturation threshold, and therefore, the sensitivity of the probe, which arises from changes in the magnetization of the nanoparticles, is a function of the external applied magnetic field. The maximum sensitivity achieved is ~11 000 pm mT^{-1}. The strong correlation among the magnetic field strength, magnetization, and refractive index of the coated nanoparticles provides firm evidence to support our

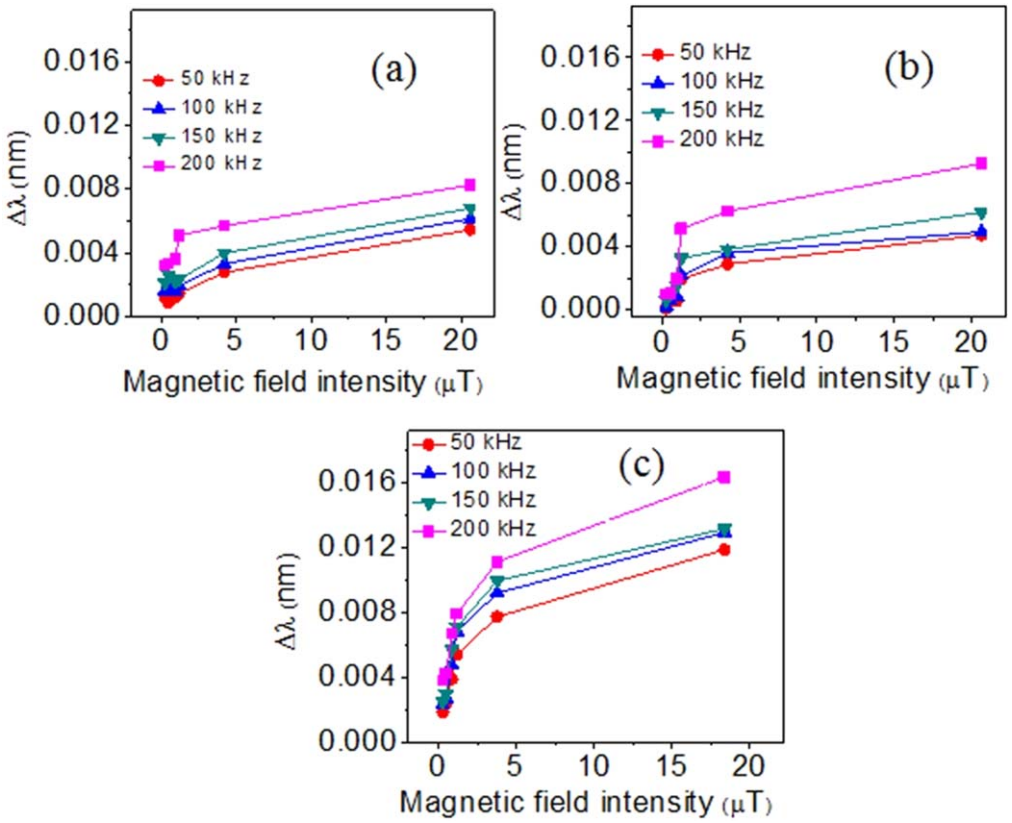

Figure 9. FBG spectrum shift with increasing magnetic field (from FBG1 to FBG6) after filling the chamber with air (a), saline solution (b), and crude oil (c).

proposed mechanism for magnetically modulating the wavelength of the propagating light.

The great importance for practical applications of magnetic sensor is time response and repeatability. Using on–off control of the magnetic field from 0 to 100 Oe a few circles of time response test was carried out, to determine the response time and the repeatability of the FBG probes. Three circles of temporal change of the reflection power reshown in figure 10. It can be seen that when the electromagnet turned off, the signal recovered to the original level. A rise and fall time according to 10% baseline to 90% signal maximum are determined as 21.2 s and 20.6 s respectively which is depicted in enlarged cycle in figure 10. The response time of the sensor mainly depends on the external magnetic field strength. The identical response behavior of the sensor confirms the high reliability and repeatability of the sensing scheme.

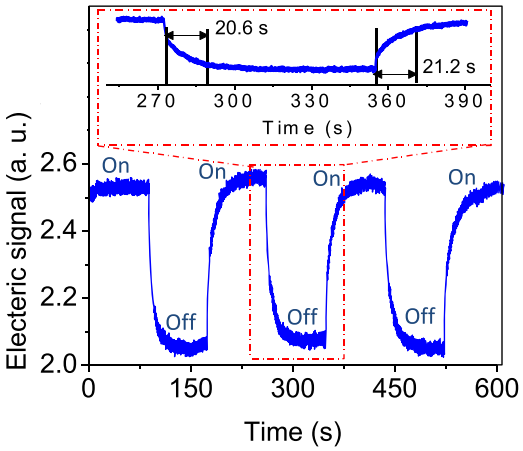

Figure 10. Time response plot of the fabricated FBG magnetic field sensor under on–off condition. The range of magnetic field is from 0 to 100 Oe.

4. Conclusion

We propose FBG fiber optic magnetic field sensors based on the magnetic features of the coated magnetite nanoparticles. The main idea of magnetic field measurement is to overcome the cross-sensitivity effect of the refractive index and magnetic field in the coated particles by understanding the interference of two modes with two different phases arising from changes in the refractive index. Six FBGs in a series configuration were fixed on the outer surface of a cylindrical glass chamber and subjected to different magnetic field strengths. The obtained shift in the wavelength in the reflection spectra for all FBGs illustrate that the proposed sensing probes are sufficiently sensitive to changes in the magnetic field, which was generated by a vertical solenoid inside the chamber. The wavelength shift observed upon changing the magnetic field decreased as an inverse cube as the distance from the solenoid increased and showed good agreement with the theoretical approach. The maximum wavelength shift was ~0.016 nm for the FBG located 15 cm away from the

solenoid axis for the chamber filled with air, and the magnetic field was ~21 μT. The sensor response time is ~21 s which approves the high reliability and repeatability of the probes. The novel design of our experiment along with the accurate fabrication of highly sensitive FBG probes may give insight into their use in the oil and gas industry, in particular, for oil movement detection.

Acknowledgment

The project was financial supported from Petroleum Research Fund through Alpha Matrix Project (Universiti Teknologi Petronas) via vote number: R.J130000.7609.4C112. The Universiti Teknologi Malaysia, AMTEC and the frontier material research alliance are acknowledged.

ORCID iDs

Alireza Samavati https://orcid.org/0000-0001-5407-6658

References

[1] Yang D, Du L, Xu Z, Jiang Y, Xu J, Wang M, Bai Y and Wang H 2014 *Appl. Phys. Lett.* **104** 061903
[2] Bao L, Dong X, Zhang S, Shen C and Shum P P 2018 *IEEE Sens. J.* **18** 4008–12
[3] Dadoenkova Y S, Bentivegna F and Moiseev S 2019 *Phys. Scr.* **94** 105006
[4] Cheng T, Zhou X and An G 2018 A novel optical-fiber magnetic field sensor based on surface plasma resonance *Optical Fiber Sensors, Optical Society of America* p TuE70
[5] Chen H, Shao Z, Zhang X, Hao Y and Rong Q 2018 *Opt. Lasers Eng.* **107** 78–82
[6] Zhao Y, Gu Y F, Lv R Q and Yang Y Y 2017 *IEEE Trans. Instrum. Meas.* **66** 502–7
[7] Lenz J E 1990 *Proc. IEEE* **78** 973–89
[8] Cruz J, Andres M and Hernandez M 1996 *Appl. Opt.* **35** 922–7
[9] Alberto N, Domingues M F, Belo J H, Marques C, Antunes P, Amaral V and André P 2019 Optical fibre fuse effect based sensor for magnetic field monitoring *Proc. SPIE* **11028** 110281S
[10] Zhao Y, Lv R Q, Wang D and Wang Q 2014 *IEEE Trans. Instrum. Meas.* **63** 2210–4
[11] He W, Yuan H, Lou X, Zhu L and Dong M 2019 *Phys. Scr.* **94** 125502
[12] Ikeda A, Nomura T, Matsuda Y H, Tani S, Kobayashi Y, Watanabe H and Sato K 2018 *Physica* B **536** 847–9
[13] Wu B, Wang M, Dong Y, Tang Y, Mu H, Li H, Yin B, Yan F and Han Z 2018 *Opt. Express* **26** 27628–38
[14] Katabira K, Yoshida Y, Masuda A, Watanabe A and Narita F 2018 *Materials* **11** 406
[15] Alberto N, Domingues M, Marques C, André P and Antunes P 2018 *Sensors* **18** 4325
[16] Zhao Y, Wu D, Lv R Q and Li J 2016 *IEEE Trans. Instrum. Meas.* **65** 1503–7
[17] Zaibudeen A and Philip J 2018 *J. Mol. Liq.* **252** 30–9
[18] Hashemizadeh A, Gholizadeh M, Tabatabaeinejad A and Hoopanah M 2014 *Pet. Sci. Technol.* **32** 1038–42
[19] Madhav K, Kumar K R, Srinivas T and Asokan S 2006 Fiber Bragg grating magnetic field sensor *2006 IEEE Instrumentation and Measurement Technology Conf. Proc. (Piscataway, NJ)* (IEEE) 2042–4
[20] Dai Y, Yang M, Xu G and Yuan Y 2013 *Opt. Express* **21** 17386–91
[21] Kashif M, Yahya N, Zaid H, Shafie A, Jasamai M, Nasir N and Akhter M 2011 *J. Appl. Sci.* **11** 1366
[22] Farley J and Price R H 2001 *Am. J. Phys.* **69** 751–4
[23] Ivakhnenko O P 2012 *Crude Oil Exploration in the World* (IntechOpen)
[24] Reitz J R, Milford F J and Christy R W 2008 *Foundations of Electromagnetic theory* (Reading, MA: Addison-Wesley)
[25] Wurtz G, Hendren W, Pollard R, Atkinson R, Le Guyader L, Kirilyuk A, Rasing T, Smolyaninov I and Zayats A 2008 *New J. Phys.* **10** 105012
[26] Wei C-M, Chen C-W, Wang C-H, Chen J-Y, Chen Y-C and Chen Y-F 2011 *Opt. Lett.* **36** 514–6
[27] Merzlikin A, Levy M, Vinogradov A, Wu Z and Jalali A 2010 *Opt. Commun.* **283** 4298–302
[28] Meschede D 2017 *Optics, Light and Lasers: the Practical Approach to Modern Aspects of Photonics and Laser Physics* (New York: Wiley) (https://doi.org/10.1002/9783527685486)
[29] Erdogan T 1998 *Opt. Commun.* **157** 249–64
[30] Sharma A K, Jha R and Gupta B 2007 *IEEE Sens. J.* **7** 1118–29